Journal of The Electrochemical Society, **156** (12) B1376-B1382 (2009)
0013-4651/2009/156(12)/B1376/7/$25.00 © The Electrochemical Society

High Temperature Crystal Chemistry and Oxygen Permeation Properties of the Mixed Ionic–Electronic Conductors $LnBaCo_2O_{5+\delta}$ (Ln = Lanthanide)

J.-H. Kim,[a] L. Mogni,[b] F. Prado,[c] A. Caneiro,[b,*] J. A. Alonso,[d] and A. Manthiram[a,*,z]

[a]*Electrochemical Energy Laboratory and Materials Science and Engineering Program, University of Texas at Austin, Austin, Texas 78712, USA*
[b]*Centro Atómico Bariloche, Comisión Nacional de Energía Atómica, San Carlos de Bariloche 8400, Argentina*
[c]*Departamento de Física, Universidad Nacional del Sur, Bahía Blanca 8000, Argentina*
[d]*Instituto de Ciencia de Materiales de Madrid, Consejo Superior de Investigaciones Cientificas, Cantoblanco, E-28049 Madrid, Spain*

The high temperature crystal chemistry and oxygen permeation properties of the cation-ordered $LnBaCo_2O_{5+\delta}$ perovskite oxides [lanthanide (Ln) = Pr, Nd, and Sm] have been investigated in comparison with the cation-disordered $La_{0.5}Ba_{0.5}CoO_{3-\delta}$ perovskite. The $LnBaCo_2O_{5+\delta}$ (Ln = Pr, Nd, and Sm) oxides exhibit a metal-insulator transition at $T < 200°C$, as evidenced by total conductivity measurements and high temperature X-ray diffraction data and an oxygen vacancy order–disorder transition at $T > 350°C$ in air, as evidenced by an orthorhombic to tetragonal transition. At a given temperature, the oxygen permeation flux decreases from Ln = La to Nd to Sm due to the changes in crystal symmetry and lattice strain. The oxygen permeation mechanism in the Ln = Nd is bulk-diffusion-limited rather than surface-exchange-limited for membrane thickness $L \geq 1.1$ mm.
 [DOI: 10.1149/1.3231501]

Manuscript submitted May 12, 2009; revised manuscript received August 23, 2009. Published October 1, 2009.

Transition metal oxides with mixed oxide-ion and electronic conducting (MIEC) properties find unique applications as oxygen separation membranes and as electrode (cathode and anode) materials in solid oxide fuel cells (SOFCs). These applications require both high electronic and oxide-ion conductivities[1,2] along with good structural and chemical stabilities[3] under the operating conditions of high temperatures and low or high oxygen partial pressures (p_{O_2}). Particularly, mixed conductors with high oxide-ion conductivity can be used as oxygen separation membranes without the use of electrodes and external circuitry required for a traditional ceramic oxygen pump. In this regard, mixed conducting oxides with perovskite or perovskite-related structures such as $Ln_{1-x}Sr_xMO_3$ (Ln = lanthanide, M = Mn, Fe, and Co),[4-8] $Ba_{1-x}Sr_x(Co,Fe)O_{3-\delta}$,[9,10] and $(La,Sr)_{n+1}M_nO_{3n+1}$ (n = 1–3 and M = Ni, Fe, and Co)[11-13] have been widely investigated as candidate materials.

In recent years, several groups have been focusing extensively on the crystal chemistry and magnetic properties of $LnBaCo_2O_{5+\delta}$ (Ln = Pr, Nd, Sm, Eu, Gd, Tb, Dy, Ho, and Y) layered perovskite oxides.[14-19] The $LnBaCo_2O_{5+\delta}$ oxides have the LnO and BaO layers alternating along the c axis, and the difference in the ionic radii between the Ln^{3+} and Ba^{2+} ions plays a dominant role in determining the oxygen content values and crystal chemistry.[18-21] For example, the oxygen content $(5 + \delta)$ value decreases with a decrease in size of the Ln^{3+} ions in the air-synthesized $LnBaCo_2O_{5+\delta}$ samples. The oxygen vacancies are localized in the LnO layer and show an ordering of the vacancies along the b axis at $\delta \sim 0.5$.[22] This oxygen vacancy ordering leads to a phase transition from tetragonal to orthorhombic structure with cell dimensions of $a_p \times 2a_p \times 2a_p$ (p refers to primitive cubic perovskite). However, recent studies have reported that the $LnBaCo_2O_{5+\delta}$ oxides with Ln = Pr and Gd lose the oxygen vacancy ordering with a structural transition from orthorhombic to tetragonal upon heating.[23,24]

The $LnBaCo_2O_{5+\delta}$ layered perovskite oxides have been gaining much attention recently due to their promising MIEC properties. Taskin et al. reported enhanced oxygen transport behavior in a layered $GdBaMn_2O_{5+\delta}$ compared to that in the disordered $Gd_{0.5}Ba_{0.5}MnO_{3-\delta}$ pervoskite.[25] The oxide-ion diffusion and surface exchange kinetics of $LnBaCo_2O_{5+\delta}$ (Ln = Pr and Gd) have been measured using an $^{18}O/^{16}O$ isotope exchange depth profile, and the results showed values comparable to those of disordered perovskite oxides.[26,27] The promising MIEC properties of $LnBaCo_2O_{5+\delta}$ (Ln = lanthanide) have stimulated the exploration of their application as cathodes in SOFCs. For instance, we showed recently that the performance of the $LnBaCo_2O_{5+\delta}$ (Ln = La, Nd, Sm, and Gd) oxides as a cathode in SOFC decreases with a decrease in size of Ln^{3+}.[20]

The SOFC performance data suggest that the overall oxygen transport rate could decrease from La to Gd in the $LnBaCo_2O_{5+\delta}$ system. Here, the Ln = La sample has a cation-disordered cubic perovskite structure ($La_{0.5}Ba_{0.5}CoO_{3-\delta}$) while the Ln = Pr, Nd, Sm, Gd, and Y samples have a cation-ordered perovskite structure ($LnBaCo_2O_{5+\delta}$). However, the oxygen transport properties of $LnBaCo_2O_{5+\delta}$ could be influenced by their high temperature structure because the ordering of oxygen vacancies impedes the oxygen transport within the lattice. Accordingly, we present here a systematic investigation of the high temperature crystal chemistry and the oxygen permeation properties of the $LnBaCo_2O_{5+\delta}$ (Ln = La, Pr, Nd, or Sm) oxides and a correlation of the oxygen permeation flux to the high temperature structures.

Experimental

The $LnBaCo_2O_{5+\delta}$ (Ln = La, Pr, Nd, and Sm) oxides were synthesized by a conventional solid-state reaction. Required amounts of the lanthanide oxides (La_2O_3, Pr_6O_{11}, Nd_2O_3, or Sm_2O_3), $BaCO_3$, and Co_3O_4 were thoroughly mixed with ethanol using an agate mortar and pestle and were calcined at 1000°C for 12 h in air. The calcined powders were then ground, pressed into pellets, and finally sintered at 1100°C for 24 h. The resulting powders were annealed at 900°C for 6 h in air, followed by slow cooling to room temperature at a rate of 1°C/min to maximize the oxygen content.

The average oxidation state of Co and the room-temperature oxygen content values in $LnBaCo_2O_{5+\delta}$ were determined by iodometric titration.[28] Thermogravimetric analysis (TGA) was carried out with a Netzsch STA 449 F3 instrument from room temperature to 900°C in both air and N_2 with a heating/cooling rate of 2°C/min. The products thus obtained were characterized by X-ray diffraction (XRD) with a Philips X'Pert equipment and Cu Kα radiation at room temperature. For high temperature XRD, samples were spread on a resistively heated platinum ribbon mounted on an Anton Paar

* Electrochemical Society Active Member.
z E-mail: rmanth@mail.utexas.edu

HTK-10 camera coupled with a Philips PW1700 diffractometer. The samples were heated with a temperature step of 100°C in the range of 20–900°C. At each step, the temperature was kept constant until no variations in the diffraction patterns were detected. A similar procedure was utilized during the cooling process as well. Rietveld refinements were carried out using the FullProf program.[29]

Oxygen permeation measurements were carried out with cointype $LnBaCo_2O_{5+\delta}$ (Ln = La, Nd, and Sm) membranes that had >90% of theoretical density. The membranes were mounted on the top of a supporting alumina tube with a Pyrex glass ring. An alumina ring with the same inner diameter as the Pyrex glass ring was also used as a weight to keep the seal leak-tight while maintaining the same permeation area on both sides of the membrane. The edge of the membrane was sealed using a glass paste. While one side of the membrane was open to air with a higher oxygen partial pressure ($p_{O_2'}$), the other side was exposed to a lower oxygen partial pressure ($p_{O_2''}$) that was controlled by regulating the helium gas flow inside the alumina tube. The resulting oxygen permeation flux (j_{O_2}) was measured with a gas chromatograph (GC, SRI 8610C). The $p_{O_2''}$ value decreases with increasing He flow, as monitored by the GC. It took several hours to obtain the equilibrium oxygen permeation flux at each $p_{O_2''}$ and temperature. Accordingly, the data presented here were collected after reaching the equilibrium j_{O_2} values. Any nitrogen detected in the carrier gas was used to correct the j_{O_2} values for air leaks.

Results and Discussion

Thermal and electrical properties of $LnBaCo_2O_{5+\delta}$.— TGA experiments were carried out in air and N_2 atmosphere as the samples were exposed to air on one side and lower oxygen partial pressures on the other side during the oxygen permeation experiments. Figure 1 shows the variations in temperature of the oxygen contents and oxidation states of cobalt in $LnBaCo_2O_{5+\delta}$ (Ln = La, Pr, Nd, and Sm) in flowing air and N_2 atmosphere. These curves were derived using the initial oxygen content values determined by the iodometric titration and the TGA data. The $LnBaCo_2O_{5+\delta}$ samples lose 0.41–0.45 oxygen atoms per formula unit upon heating to 900°C in air (Fig. 1a). The amount of oxygen loss increases from 0.55 to 0.60 per formula unit upon changing the atmosphere to N_2 (Fig. 1b). Although the amount of oxygen loss does not vary significantly with going from Ln = La to Sm in $LnBaCo_2O_{5+\delta}$ (both in air and N_2 atmosphere), the oxidation state of cobalt ions at a given temperature decreases significantly from Ln = La to Sm due to a decrease in initial room-temperature oxygen content values. The Ln = La sample shows a linear slope in the TGA curves in both air and N_2 at $T > 300$°C, while the Ln = Pr, Nd, and Sm samples show a slight variation in slopes especially in N_2 atmosphere, which could be related to structural transitions.

Figure 2 shows the variations in the total electrical conductivity of $LnBaCo_2O_{5+\delta}$ with temperature. For the Ln = Sm sample, the sudden drop in conductivity at $T < 200$°C is characteristic of a metal-insulator (*M-I*) transition, which occurs due to an ordering of the low spin $Co^{III}(t_{2g}^6 e_g^0)$ and intermediate spin $Co^{iii}(t_{2g}^5 e_g^1)$ ions.[14,15] This *M-I* transition becomes less pronounced in the Ln = Nd and Pr samples and finally disappears in the Ln = La sample due to the increasing oxidation state of cobalt and the consequent decrease in the oxide-ion vacancy concentration and increase in the Co–O covalency and bandwidth.[30-32] All the samples show a decrease in electrical conductivity with increasing temperature $T > 200$°C due to an increasing concentration of oxygen vacancies. For the same reason, at a given temperature, the electrical conductivity decreases from Ln = La to Sm due to an increasing concentration of oxygen vacancies. However, as the temperature increases, the difference between the electrical conductivity values of the cation-disordered cubic (Ln = La) and the cation-ordered layered perovskites (Ln = Pr, Nd, and Sm) tends to decrease, and the electrical conductivity values at ~900°C are in the range of 400–750 S/cm irrespective of the Ln^{3+} ions.

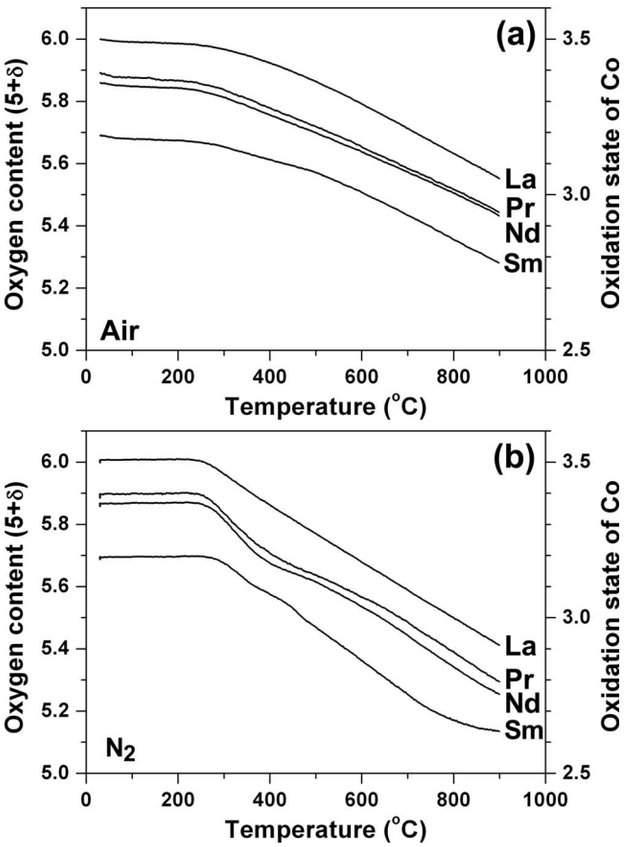

Figure 1. Variations in the oxygen content and the oxidation state of cobalt in $LnBaCo_2O_{5+\delta}$ (Ln = La, Pr, Nd, Sm) with temperature in (a) air and (b) nitrogen atmosphere with a $p_{O_2} \approx 10^{-5}$ atom.

Structural transitions in $LnBaCo_2O_{5+\delta}$ (Ln = Pr, Nd, Sm).— Figures 3-6 show the high temperature XRD patterns and lattice parameter variation in the Ln = Pr and Nd samples in the temperature range of 20–900°C in air. Both the samples have a tetragonal structure (space group *P*4/*mmm*) at 20°C. A recent study on the room-temperature crystallographic structure of the Ln = Pr samples

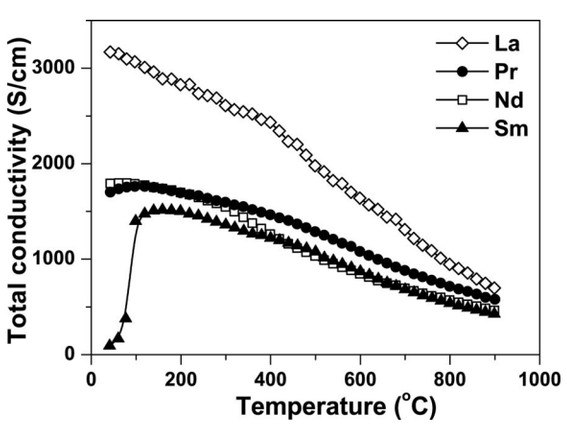

Figure 2. Temperature dependence of the total conductivity of $LnBaCo_2O_{5+\delta}$ (Ln = La, Pr, Nd, Sm) in air.

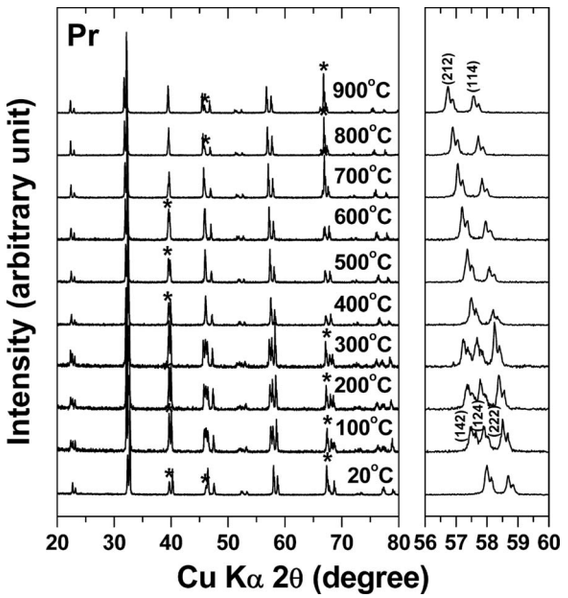

Figure 3. High temperature XRD patterns of $PrBaCo_2O_{5+\delta}$ recorded with increasing temperature in air. An expanded view in the range of $56° \leq 2\theta \leq 60°$ is displayed in the right panel. Reflections marked with an asterisk belong to Pt from the sample stage.

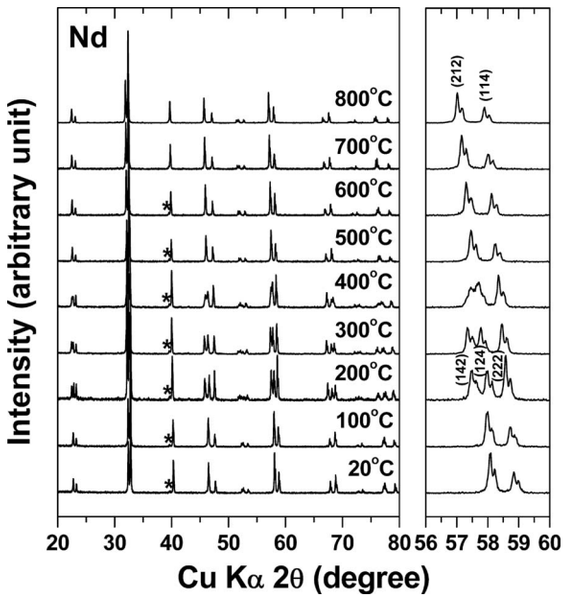

Figure 5. High temperature XRD patterns of $NdBaCo_2O_{5+\delta}$ recorded with increasing temperature in air. An expanded view in the range of $56° \leq 2\theta \leq 60°$ is displayed in the right panel. Reflections marked with an asterisk belong to Pt from the sample stage.

reported different phases depending on the oxygen content value.[22] For example, the Ln = Pr sample with $(5 + \delta) \approx 5.5$ showed oxygen vacancy ordering along the *b* axis with an orthorhombic (space group *Pmmm*) cell dimensions of $a_p \times 2a_p \times 2a_p$. Similarly, an earlier study on the Ln = Nd sample with $(5 + \delta) = 5.69$ also suggested it to be orthorhombic (space group *Pmmm*).[17] In our study, the Ln = Pr and Nd samples have higher room-temperature oxygen contents $(5 + \delta)$ of, respectively, 5.89 and 5.85 after annealing at 900°C in air and show a tetragonal structure (space group *P*4/*mmm*) with cell dimensions of $a_p \times a_p \times 2a_p$ (Fig. 3 and 5). Likely, the high oxygen content values (close to 6.0) of the Ln = Pr and Nd samples may destroy the ordering of oxygen vacancies, resulting in a tetragonal structure. For example, the XRD pattern of the Ln = Sm sample with an oxygen content of 5.69 shows a distinct peak splitting at 20°C, which could be indexed on the basis of an orthorhombic (space group *Pmmm*) structure, as shown in Fig. 7. However, the low X-ray scattering factor of oxygen atoms compared to those of the heavier Ba and Ln atoms hinders us from observing the subtle orthorhombic distortion even if there is a weak ordering of oxygen vacancies. Future neutron diffraction studies will be helpful in observing the ordering of oxygen vacancies.

The XRD data of the Ln = Pr and Nd samples show the splitting of the (212) peak into (142) and (124) peaks, which belong to an orthorhombic (space group *Pmmm*) phase, with increasing temperature from 20 to 200°C. This orthorhombic distortion has been explained to be related to the *M-I* transition, as observed from the electrical conductivity data in Fig. 2.[19,23] Further increase in temperature leads to another phase transition from orthorhombic to tetragonal (space group *P*4/*mmm*) in both the Ln = Pr and Nd samples. Expanded views in Fig. 3 and 5 show that the (142) and (124) peaks of the orthorhombic phase merge again into a tetragonal

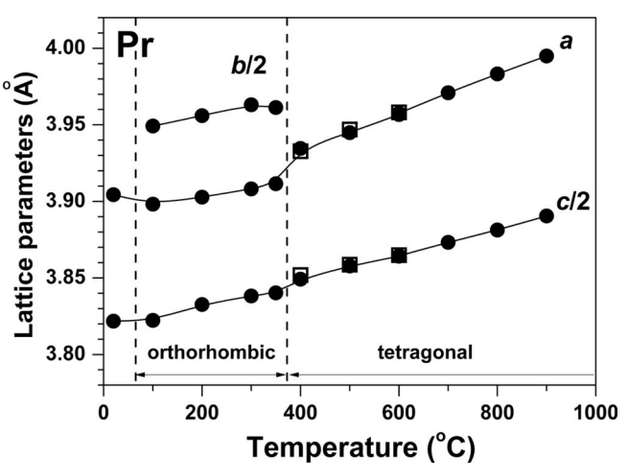

Figure 4. Variations in the lattice parameters of $PrBaCo_2O_{5+\delta}$ with temperature. The data were collected during heating (closed symbol) and cooling (open symbol) in air.

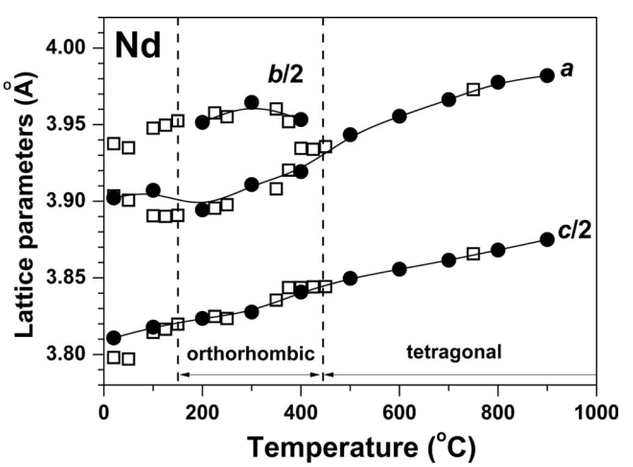

Figure 6. Variations in the lattice parameters of $NdBaCo_2O_{5+\delta}$ with temperature. The data were collected during heating (closed symbol) and cooling (open symbol) in air.

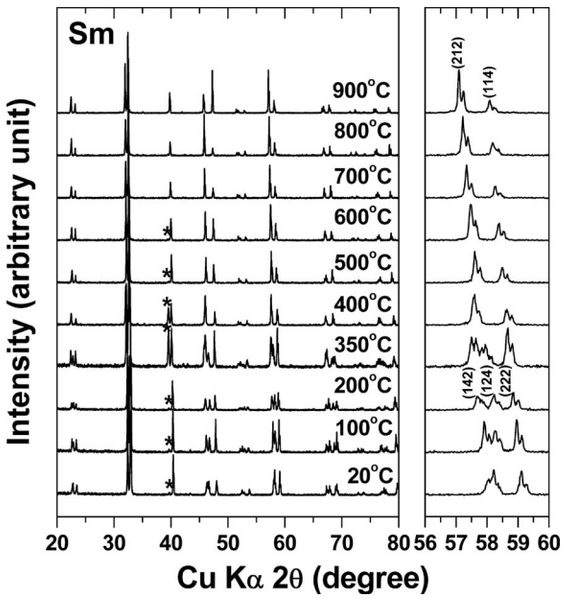

Figure 7. High temperature XRD patterns of $SmBaCo_2O_{5+\delta}$ recorded with increasing temperature in air. An expanded view in the range of $56° \leq 2\theta \leq 60°$ is displayed in the right panel. Reflections marked with an asterisk belong to Pt from the sample stage.

(212) peak at 400°C for the Ln = Pr sample and at 500°C for the Ln = Nd sample. Streule et al.[23] explained this to be due to the thermally activated order–disorder transition with a phase transition from orthorhombic to tetragonal.[23] This high temperature tetragonal phase (space group *P*4/*mmm*) is observed up to 900°C in air.

Figures 4 and 6 show the variation in the lattice parameters with temperature, respectively, for the Ln = Pr and Nd samples on heating and cooling in air. The oxygen loss upon heating results in a reduction in the cobalt ions in $LnBaCo_2O_{5+\delta}$ (Fig. 1) and a consequent increase in the lattice parameters. Especially, the high temperature phase transitions accompanying the *M-I* transitions and oxygen vacancy order–disorder transition lead to sudden variations in the lattice parameters *a* and *b*. Figure 6 shows that the oxygen vacancy order–disorder transition in the Ln = Nd sample is reversible at $T \sim 450$°C upon heating/cooling. However, the XRD pattern of the Nd sample recorded at room temperature after the cooling process showed well-separated peaks corresponding to an orthorhombic distortion with a clear deviation between the *a* and *b* parameters. Although this may appear inconsistent with the clear tetragonal structure observed with the starting material (Fig. 5), it could be understood by considering the following. In our high temperature XRD experiments, the cooling rate was not controlled, and the Nd sample was cooled rapidly to a lower temperature. As a result, the Ln = Nd sample after the high temperature XRD experiment had a lower oxygen content value after cooling to 20°C due to the insufficient oxygen uptake during cooling compared to the starting sample ($5 + \delta = 5.85$). For example, the XRD pattern of the Ln = Nd sample recorded after the TGA measurement with a slow heating/cooling rate of 2°C/min in air shows the same tetragonal phase as the $NdBaCo_2O_{5.85}$.

Figure 7 shows the high temperature XRD patterns of the Ln = Sm sample upon heating in air. With an oxygen content of 5.69, the Ln = Sm sample has the orthorhombic structure (space group *Pmmm*) at 20°C. At $100°C \leq T \leq 200°C$, the splitting between the (142) and (124) peaks increases (Fig. 7) with an increasing gap between *a* and *b*/2 in Fig. 8. This increase in orthorhombicity is accompanied by the *M-I* transition, as observed in Fig. 2. The Ln = Sm sample also shows a phase transition from orthorhombic to tetragonal at $T \sim 400$°C.

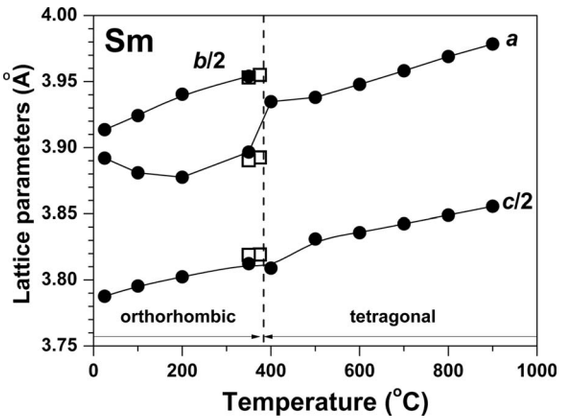

Figure 8. Variations in the lattice parameters of $SmBaCo_2O_{5+\delta}$ with temperature. The data were collected during heating (closed symbol) and cooling (open symbol) in air.

To assess the structural stability of the $LnBaCo_2O_{5+\delta}$ (Ln = La, Pr, Nd, and Sm) layered perovskites under N_2, we have refined the crystal structure of the samples obtained after the TGA measurements in N_2. Table I gives the room-temperature oxygen content $(5 + \delta)$ values obtained by iodometric titration and the crystallographic data of these samples. After the TGA experiment in N_2, the Ln = La sample has an oxygen content $(5 + \delta)$ of 5.46 and maintains the original cubic structure with the space group $Pm\bar{3}m$, as evidenced by a good agreement between the observed and calculated profiles in Fig. 9. The Ln = Pr, Nd, and Sm samples, however, have oxygen contents of, respectively, 5.36, 5.30, and 5.18 with a tetragonal structure (space group *P*4/*mmm*) due to the loss of oxygen vacancy ordering. However, the Ln = Nd sample shows additional reflections (e.g., a shoulder at $2\theta \approx 46.5°$) in the XRD pattern corresponding to a secondary phase. A similar secondary phase has also been observed in the $NdBaCo_2O_{5.38}$ sample, and it has been refined to be $NdBaCo_2O_{5.5}$.[17] Therefore, the XRD pattern of the Ln = Nd sample was refined based on $NdBaCo_2O_{5.30}$ (space group *P*4/*mmm*) and $NdBaCo_2O_{5.50}$ (space group *Pmmm*) phases, and their Bragg peak positions are marked individually in Fig. 9. The amount of the $NdBaCo_2O_{5.50}$ secondary phase was calculated to be 30%. All the XRD patterns in Fig. 9 indicate that the $LnBaCo_2O_{5+\delta}$ samples are stable under N_2 atmosphere of up to 900°C.

Table I. Room-temperature oxygen contents and crystallographic data after the TGA measurements in N_2 atmosphere of $LnBaCo_2O_{5+\delta}$ (Ln = La, Pr, Nd, Sm). [For the cubic structure ($Pm\bar{3}m$), the atomic positions are (Ln, Ba) (0,0,0), Co (1/2,1/2,1/2), O (0,1/2,1/2). For the tetragonal structure (*P*4/*mmm*), the atomic positions are Ln (0,0,1/2), Ba (0,0,0), Co (1/2,1/2,*z*), O1 (1/2,1/2,0), O2 (1/2,0,*z*), and O3 (1/2,1/2,1/2).]

Ln	La	Pr	Nd[a]	Sm
Oxygen contents $(5 + \delta)$	5.46	5.36	5.30	5.18
Space group	$Pm\bar{3}m$	*P*4/*mmm*	*P*4/*mmm*	*P*4/*mmm*
a (Å)	3.940	3.946	3.939	3.928
c (Å)	—	7.610 (1)	7.576	7.540
Co(*z*)	—	0.248 (1)	0.254 (1)	0.255 (1)
O2(*z*)	—	0.294 (1)	0.303	0.306 (1)
R_p	8.03	8.01	7.91	9.53
R_{wp}	10.9	10.5	10.5	12.3
χ^2	1.78	1.52	2.03	2.55

[a] The Ln = Nd sample has 30% of $NdBaCo_2O_{5.50}$ as a secondary phase.

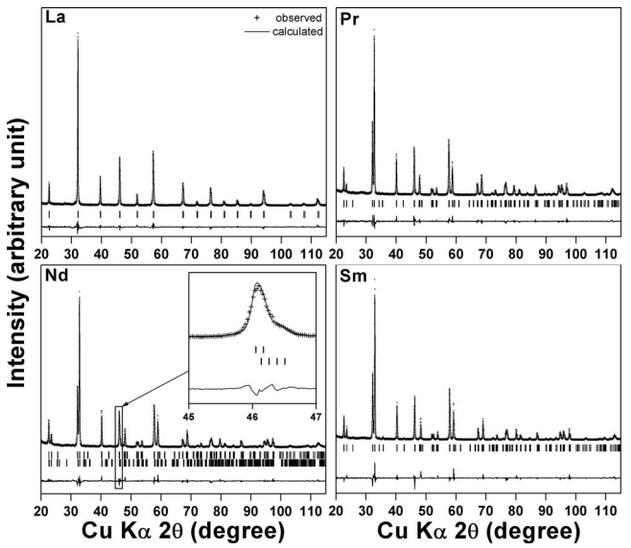

Figure 9. Room-temperature XRD patterns, calculated profiles, peak positions, and the difference between the observed and calculated profiles of the $LnBaCo_2O_{5+\delta}$ (Ln = La, Pr, Nd, and Sm) samples after the TGA experiments in N_2 atmosphere. For the Ln = Nd sample, the upper peak positions belong to $NdBaCo_2O_{5.30}$ (space group *P*4/*mmm*) while the lower peak positions belong to $NdBaCo_2O_{5.50}$ (space group *Pmmm*).

Oxygen permeation properties of $LnBaCo_2O_{5+\delta}$ (Ln = La, Nd, and Sm).— Figure 10 compares the variations in the oxygen permeation flux (j_{O_2}) through the $LnBaCo_2O_{5+\delta}$ (Ln = La, Nd, and Sm) ceramic membranes as a function of (p_{O_2}'/p_{O_2}''). All three membranes had the same 1.1 mm thickness (L). The experiments were carried out by adjusting the helium flow rate to vary the p_{O_2}'' on one side of the sample (inside the ceramic tube) while the other side was exposed to air ($p_{O_2}' = 0.209$ atom). All three membranes show an increase in j_{O_2} with temperature due to the increasing amount of oxygen vacancies (Fig. 1) and increasing oxide-ion conductivity, as has been observed with other perovskite systems.[33] At a given temperature, the j_{O_2} value decreases from Ln = La to Nd to Sm, as seen in Fig. 10.

Figure 11 compares the temperature dependence of $\log(j_{O_2})$ in the Ln = La, Nd, and Sm membranes having the same 1.1 mm thickness (L) at $\log(p_{O_2}'/p_{O_2}'') = 1.0$ and 1.5. The data for the Ln = Nd specimen with $L = 3.3$ mm are also plotted in Fig. 11 for comparison. Although slight deviations in the slope occur due to small variations in the sample thickness and density, it can be concluded that all the samples have similar activation energies for oxygen permeation in the temperature range of 700–900°C.

To understand the oxygen permeation mechanism, the oxygen flux through the Ln = Nd membranes with different thicknesses (L) of 1.1, 1.8, and 3.3 mm were measured (Fig. 12). When the oxygen permeation through a mixed ionic–electronic conductor is limited by a surface exchange rate, j_{O_2} does not vary with the thickness of the membrane. However, if the oxygen permeation is bulk limited, j_{O_2} across the membrane varies with the thickness of the membrane in accordance with the Wagner equation[34]

$$j_{O_2} = \frac{RT}{4^2F^2L}\int_{\ln p_{O_2}'}^{\ln p_{O_2}''} \frac{\sigma_{el}\sigma_{ion}}{\sigma_{el}+\sigma_{ion}} d \ln p_{O_2} \qquad [1]$$

where R is the gas constant, F is the Faraday constant, T is the temperature, L is the thickness of the membrane, and σ_{el} and σ_{ion} are, respectively, the electronic and ionic conductivities. Figure 12a shows that the j_{O_2} decreases with increasing L at 900 and 870°C.

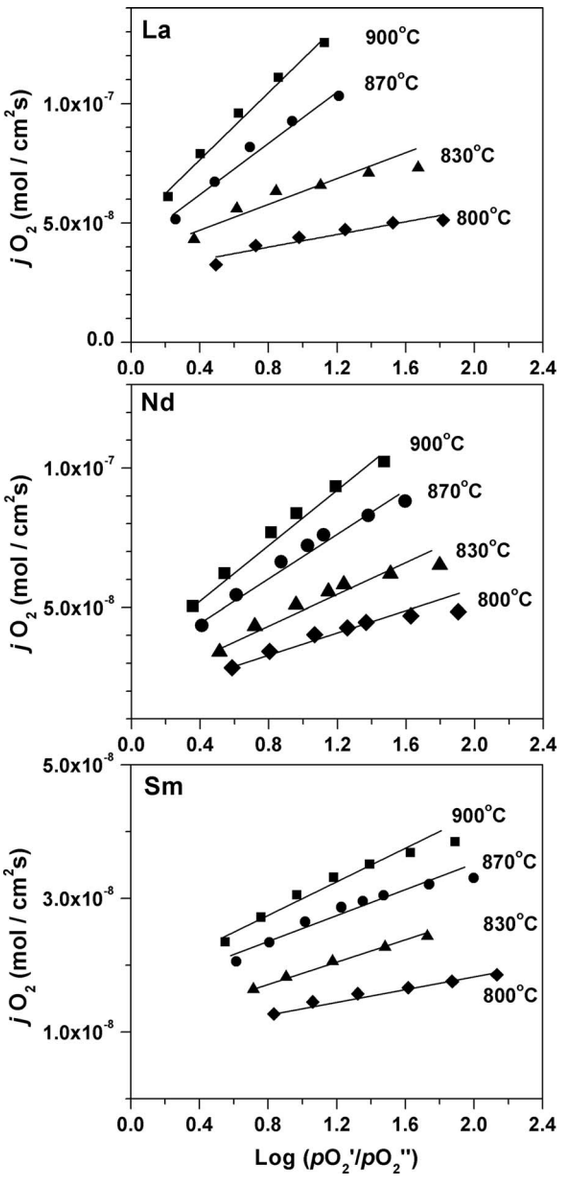

Figure 10. Variations in the oxygen permeation flux (j_{O_2}) of $LnBaCo_2O_{5+\delta}$ (Ln = La, Nd, and Sm) with $\log(p_{O_2}'/p_{O_2}'')$ at different temperatures. The measurements were conducted in 1.1 mm thick samples.

The variations in j_{O_2} with the reciprocal of membrane thickness ($1/L$) exhibit a linear relationship and good extrapolation to the origin in Fig. 12b. These results suggest that the rate of oxygen permeation in the $LnBaCo_2O_{5+\delta}$ samples is governed by bulk diffusion rather than surface exchange for $L \geq 1.1$ mm. Based on the observed high total conductivity $\sigma_{total} > 400$ S/cm for the $LnBaCo_2O_{5+\delta}$ (Ln = La, Nd, and Sm) samples at $T \leq 900$°C (Fig. 2) and the recognition that perovskite oxides generally exhibit $\sigma_{el} \gg \sigma_{ion}$, Eq. 1 can be further simplified as

$$j_{O_2} = \frac{RT}{4^2F^2L}\bar{\sigma}_{ion} \ln(p_{O_2}'/p_{O_2}'') \qquad [2]$$

Using Eq. 2 and the experimental data in Fig. 10, one can obtain the average ionic conductivity values for the $LnBaCo_2O_{5+\delta}$ (Ln = La, Nd, and Sm) samples. The data in Table II reveal that the σ_{ion} values decrease with decreasing Ln^{3+} size and temperature.

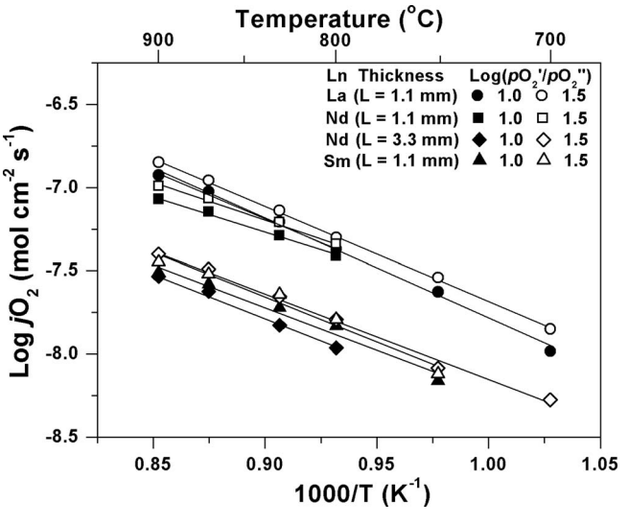

Figure 11. Arrhenius plots of the variations in the oxygen permeation flux (j_{O_2}) of $LnBaCo_2O_{5+\delta}$ (Ln = La, Nd, and Sm) with inverse temperature at $\log(p_{O_2'}/p_{O_2''}) = 1.0$ and 1.5.

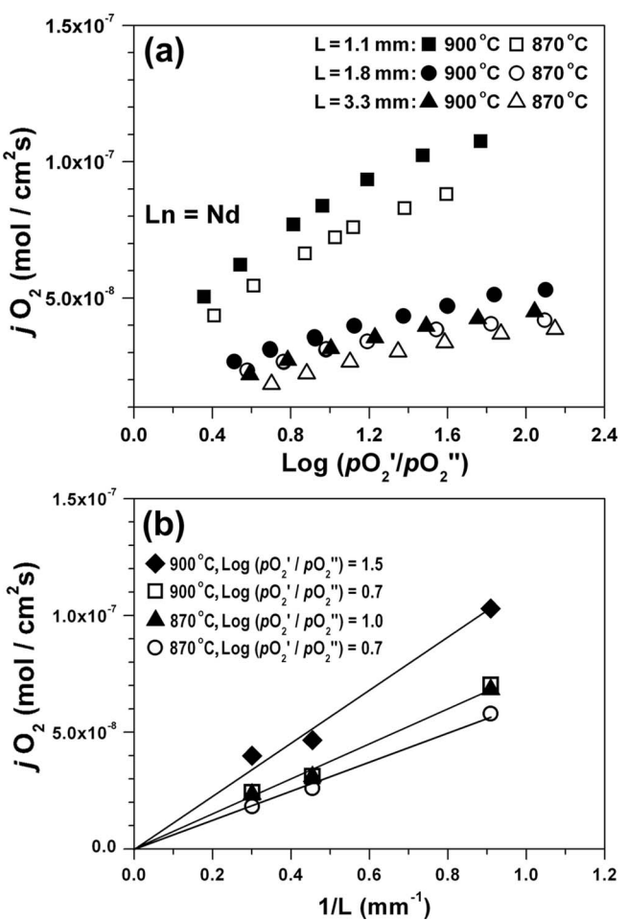

Figure 12. (a) Variations in the oxygen permeation flux (j_{O_2}) of $NdBaCo_2O_{5+\delta}$ with $\log(p_{O_2'}/p_{O_2''})$ for different sample thicknesses (L) and (b) variations in the oxygen permeation flux (j_{O_2}) of $NdBaCo_2O_{5+\delta}$ with inverse sample thickness ($1/L$).

Table II. Transport data of $LnBaCo_2O_{5+\delta}$.

Temperature	Ln	σ_{ion} (S cm^{-1})	D_v (cm^2 s^{-1})	σ_{total} (S cm^{-1})	$\sigma_{ion}/\sigma_{total}$ ($\times 10^5$)
900°C	La	0.056	1.86×10^{-6}	700	8.0
	Nd	0.04	1.03×10^{-6}	464	8.6
	Sm	0.011	2.45×10^{-7}	425	2.6
870°C	La	0.046	1.56×10^{-6}	767	6.0
	Nd	0.037	9.63×10^{-7}	497	7.4
	Sm	0.01	2.18×10^{-7}	450	2.2

The oxygen diffusion in the layered $LnBaCo_2O_{5+\delta}$ perovskites is expected to occur via a vacancy transport mechanism similar to that observed in the disordered perovskites. Because the oxygen vacancies occur predominantly in the LnO planes of the layered perovskites, oxygen vacancies (V) could be transported to the next available site (O3) via two possible oxygen sites (O2), as indicated by the arrows in Fig. 13. Although oxygen (O1) in the BaO plane may not participate in the oxygen vacancy hopping, the approximate vacancy diffusion coefficient (D_v) in comparison with the disordered perovskite (Ln = La) has been calculated by employing the Nernst–Einstein equation

$$\sigma_{ion} = \frac{4F^2[V_O^{\bullet\bullet}]D_v}{RTV_mN_A} \quad [3]$$

where $[V_O^{\bullet\bullet}]$ is the vacancy concentration, V_m is the perovskite molar volume, and N_A is Avogadro's number. At a given temperature, the approximate D_v value decreases from Ln = La to Nd to Sm in Table II.

The bulk diffusion process of oxygen is closely related to the crystal structures. For example, the oxygen diffusion pathway is

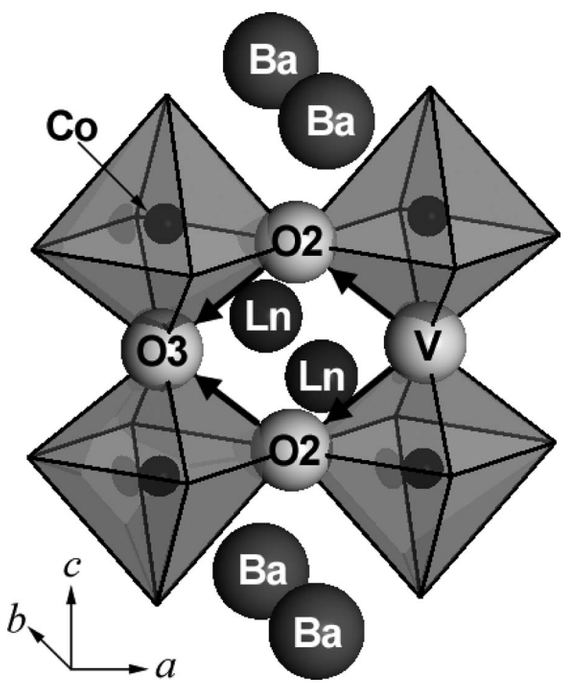

Figure 13. Illustration of the oxygen vacancy transport in the $LnBaCo_2O_{5+\delta}$ lattice with the tetragonal structure ($P4/mmm$). The atomic positions are Ln (0,0,1/2), Ba (0,0,0), Co (1/2,1/2,z), O1 (1/2,1/2,0), O2 (1/2,0,z), and O3 (1/2,1/2,1/2). V refers to oxygen vacancy, and the arrows indicate their hopping direction toward a neighboring site (O3). Some of the atoms are omitted for simplicity.

Table III. The atomic positions in $LnBaCo_2O_{5+\delta}$ at 800°C. [based on the tetragonal structure (*P4/mmm*) with atomic positions of Ln (0,0,1/2), Ba (0,0,0), Co (1/2,1/2,*z*), O1 (1/2,1/2,0), O2 (1/2,0,*z*), and O3 (1/2,1/2,1/2).]

Sample	*a* (Å)	*c* (Å)	Co(*z*)	O2(*z*)	χ^2
$NdBaCo_2O_{5+\delta}$	3.977	7.737	0.252(1)	0.295(1)	1.78
$SmBaCo_2O_{5+\delta}$	3.968	7.698	0.256(2)	0.319(3)	1.60

three-dimensional in the Ln = La sample having a disordered perovskite structure due to the smaller size difference between La^{3+} and Ba^{2+}. In contrast, the oxygen diffusion is expected to be two-dimensional in both the Ln = Nd and Sm samples having a tetragonal structure (space group *P4/mmm*) at $T > 500$°C (Fig. 5-8), in which the oxygen vacancies are localized in the LnO plane due to a larger size difference between Ln^{3+} and Ba^{2+}. Mogensen et al.[35] proposed that the degree of lattice distortion is the critical factor that governs the ionic conductivity after reviewing various oxide-ion conductors. Following this criterion, the Ln = La sample with the cubic perovskite structure exhibits a higher oxide-ion conductivity or j_{O_2} due to less lattice distortion compared to the Ln = Nd and Sm samples with tetragonal structures. For the same reason, the Ln = Nd sample shows higher oxide-ion conductivity or j_{O_2} compared to the Ln = Sm sample. Table III shows the atomic positions of the Ln = Nd and Sm samples at 800°C obtained from the Rietveld refinement of the high temperature XRD patterns. The Co(*z*) and O2(*z*) atomic positions in both the Ln = Nd and Sm samples deviated from the ideal position (0.25 for the cubic perovskite) due to the large size difference between the Ln^{3+} and Ba^{2+} ions. Between the Ln = Nd and Sm samples, the Ln = Sm sample exhibits a larger deviation due to the larger size difference between Sm^{3+} and Ba^{2+} compared to that between Nd^{3+} and Ba^{2+}, which results in a larger lattice distortion and consequently lower ionic conductivity or j_{O_2}. Similarly, it has been reported that the larger Ln = Pr shows a higher oxygen diffusion rate compared to the smaller Ln = Gd in the $LnBaCo_2O_{5+\delta}$.[26]

Conclusions

The high temperature structures and oxygen permeation properties of $LnBaCo_2O_{5+\delta}$ oxides have been investigated. The $LnBaCo_2O_{5+\delta}$ (Ln = Pr, Nd, and Sm) oxides exhibit *M-I* transitions at $T < 200$°C and oxygen vacancy order–disorder transitions accompanied by a transition from orthorhombic to tetragonal structure at $T > 350$°C. At a given temperature, the oxygen permeation flux j_{O_2} through the $LnBaCo_2O_{5+\delta}$ membranes decreases from La to Nd to Sm due to a lowering of the crystal symmetry and lattice strain. A linear dependence of j_{O_2} with the reciprocal of membrane thickness $(1/L)$ and its extrapolation to the origin in the Ln = Nd sample reveals that the oxygen transport mechanism is bulk-diffusion-limited. The oxide-ion conductivity values calculated using Wagner's equation decrease with a decrease in size of the Ln^{3+} ions from Ln = La to Nd to Sm.

Acknowledgments

Financial support from the Welch Foundation (grant F-1254), Argentine Research Council (CONICET), and ANPCyT (no. PICT 06-16-829 and no. 07-16-2288) in Argentina is gratefully acknowledged.

University of Texas assisted in meeting the publication costs of this article.

References

1. D. J. L. Brett, A. Atkinson, N. P. Brandon, and S. J. Skinner, *Chem. Soc. Rev.*, **37**, 1568 (2008).
2. N. Q. Minh and T. Takahashi, *Science and Technology of Ceramic Fuel Cells*, Chaps. 4 and 5, p. 117, Elsevier, Amsterdam (1995).
3. H. J. M. Bouwmeestere and A. J. Burggraaf, in *The CRC Handbook of Solid State Electrochemistry*, Chap. 14, P. J. Gellings and H. J. M. Bouwmeestere, Editors, CRC, New York (1997).
4. M. A. Señarís-Rodríguez and J. B. Goodenough, *J. Solid State Chem.*, **118**, 323 (1995).
5. H. Ullmann, N. Trofimenco, F. Tietz, D. Stöver, and A. Ahmad-Khanlou, *Solid State Ionics*, **138**, 79 (2000).
6. Y. Teraoka, T. Nobunaga, and N. Yamazoe, *Chem. Lett.*, **1988**, 503.
7. J.-M. Bae and B. C. H. Steele, *Solid State Ionics*, **106**, 247 (1998).
8. K. T. Lee and A. Manthiram, *Solid State Ionics*, **176**, 1521 (2005).
9. Z. Shao and S. M. Haile, *Nature (London)*, **431**, 170 (2004).
10. B. Wei, Z. Lü, X. Huang, J. Miao, X. Sha, X. Xin, and W. Su, *J. Eur. Ceram. Soc.*, **26**, 2827 (2006).
11. A. Manthiram, F. Prado, and T. Armstrong, *Solid State Ionics*, **152–153**, 647 (2002).
12. J. A. Kilner and C. K. M. Shaw, *Solid State Ionics*, **154–155**, 523 (2002).
13. L. Mogni, F. Prado, and A. Caneiro, *Chem. Mater.*, **18**, 4163 (2006).
14. C. Martin, A. Maignan, D. Pelloquin, N. Nguyen, and B. Raveau, *Appl. Phys. Lett.*, **71**, 1421 (1997).
15. Y. Moritomo, M. Takeo, X. J. Liu, T. Akimoto, and A. Nakamura, *Phys. Rev. B*, **58**, R13334 (1998).
16. T. Vogt, P. M. Woodward, P. Karen, B. A. Hunter, P. Henning, and A. R. Moodenbaugh, *Phys. Rev. Lett.*, **84**, 2969 (2000).
17. J. C. Burley, J. F. Mitchell, S. Short, D. Miller, and Y. Tang, *J. Solid State Chem.*, **170**, 339 (2003).
18. I. O. Troyanchuk, N. V. Kasper, and D. D. Khalyavin, *Phys. Rev. B*, **58**, 2418 (1998).
19. A. Maignan, C. Martin, D. Pelloquin, N. Nguyen, and B. Raveau, *J. Solid State Chem.*, **142**, 247 (1999).
20. J.-H. Kim and A. Manthiram, *J. Electrochem. Soc.*, **155**, B385 (2008).
21. J.-H. Kim, F. Prado, and A. Manthiram, *J. Electrochem. Soc.*, **155**, B1023 (2008).
22. C. Frontera, A. Caneiro, A. E. Carrillo, J. Oró-Solé, and J. L. García-Muñoz, *Chem. Mater.*, **17**, 5439 (2005).
23. S. Streule, A. Podlesnyak, D. Sheptyakov, E. Pomjakushina, M. Stingaciu, K. Conder, M. Medarde, M. V. Patrakeev, I. A. Leonidov, V. L. Kozhevnikov, et al., *Phys. Rev. B*, **73**, 094203 (2006).
24. A. Tarancón, D. Marrero-López, J. Peña-Martínez, J. C. Ruiz-Morales, and P. Núñez, *Solid State Ionics*, **179**, 611 (2008).
25. A. A. Taskin, A. N. Lavro, and Y. Ando, *Appl. Phys. Lett.*, **86**, 091910 (2005).
26. G. Kim, S. Wang, A. J. Jacobson, L. Reimus, P. Brodersen, and C. A. Mims, *J. Mater. Chem.*, **17**, 2500 (2007).
27. A. Tarancón, S. J. Skinner, R. J. Chater, F. H. Ramírez, and J. A. Kilner, *J. Mater. Chem.*, **17**, 3175 (2007).
28. A. Manthiram, J. S. Swinnea, Z. T. Sui, H. Steinfink, and J. B. Goodenough, *J. Am. Chem. Soc.*, **109**, 6667 (1987).
29. J. Rodriguez-Carvajal, *Physica B*, **192**, 55 (1993).
30. H. Takahashi, F. Munakata, and M. Yamanaka, *Phys. Rev. B*, **57**, 15211 (1998).
31. K. T. Lee and A. Manthiram, *J. Electrochem. Soc.*, **152**, A197 (2005).
32. K. T. Lee and A. Manthiram, *J. Electrochem. Soc.*, **153**, A794 (2006).
33. H. J. M. Bouwmeester, H. Kruidhof, and A. J. Burggraaf, *Solid State Ionics*, **72**, 185 (1994).
34. C. Wagner, *Prog. Solid State Chem.*, **10**, 3 (1975).
35. M. Mogensen, D. Lybye, N. Bonanos, P. V. Hendriksen, and F. W. Poulsen, *Solid State Ionics*, **174**, 279 (2004).